Final Report for:
Human Electro-Muscular Incapacitation (HEMI): Physiological Modeling Weapons

Revision 1

2 April 2018

Prepared for:
Joint Non-Lethal Weapons Directorate
3097 Range Road
Quantico , VA 22134-5100
c/o Dr. Shannon Foley

Prepared by:
Applied Research Associates, Inc.
Arlington Division
801 N. Quincy Street, Suite 700
Arlington, VA 22203

Authors: Owen Price, Bahman Asgharian, Jacob Bellman, and Daniela Stricklin

Reviewer: Steve Beaulieu

Contracts W911NF-12-C-0067 and W911NF-17-D-0006-0001-04

Table of Contents

List of Figures

HEMI Physiological Modeling

1. Background

Human Electro-Muscular Incapacitation (HEMI) weapons are developed with the intent to incapacitate a subject without being lethal. However, under some use cases, these weapons have been linked to serious injury and even death (Cooks et al., 2016; Dawes et al., 2011; Gleason & Ahmad, 2015; Ho & Dawes, 2011; Sanford, Jacobs, Roe, & Terndrup, 2011). ARA has been developing a generalized computational model based on underlying physical and biological processes, which will use device characteristics and potential military exposure scenarios as inputs. The goal of this research is to develop a product that estimates the risks of rhabdomyolysis, cardiovascular, and respiratory effects under different use scenarios or with different device characteristics. This will be accomplished through mathematical models that estimate a dose metric for a given HEMI exposure, and use the dose to evaluate the risk of injury for the physiological system under examination (Figure 1).

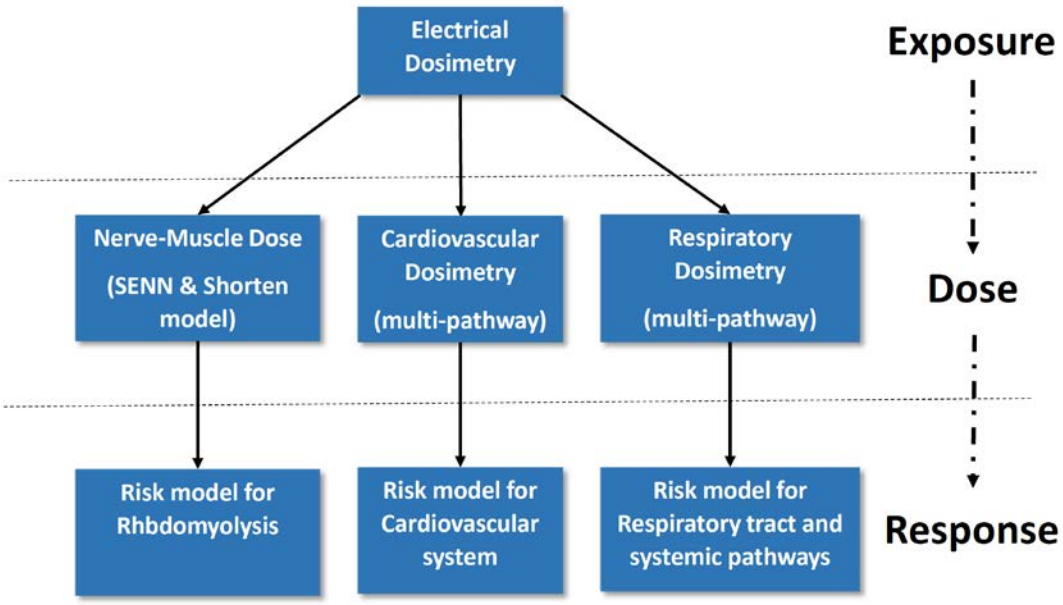

Figure 1. General approach for the HEMI physiological modeling project.

Many studies addressing the pathophysiological effects resulting from electrical stimulation devices have linked overstimulation with rhabdomyolysis. In the initial phase of this project, our focus was on identifying the mechanisms of rhabdomyolysis from HEMI exposures and mechanistic models which could inform the estimation of rhabdomyolysis risk. Rhabdomyolysis is the destruction of muscle cells that leads to the toxic cell contents being released into the blood stream. The dynamics of rhabdomyolysis are not fully understood, but specific mechanisms have been identified as potential precursors to rhabdomyolysis. In particular, ATP depletion and calcium buildup in the muscle cell myoplasm have been attributed to overstimulation of the cell

membrane by the external electrical current. To establish a mechanistic-based model for rhabdomyolysis, we have begun development of models that describe the electrical current in the body, motor neuron excitation, and muscle cell contraction. Once developed, an integrated version of these models will describe the exposure and the downstream consequences of muscle overstimulation.

2. Electrical Dosimetry

The first step in assessing human body tissue response to a discharge from a HEMI device is to determine the electric field and potential (voltage) generated within the body. For prediction of respiratory, cardiac, renal, and other risk endpoints, the electrical dose received by the body must be estimated. The magnitude of the electric field inside the body depends directly on the distance from the HEMI device electrodes. Variation of the electric field within the body may lead to disparity in tissue response because a threshold electric field is required to induce a response within the body. The main objective in this task was to establish methods for calculating the electric field and identify the tissues with electric field magnitudes above the threshold necessary to elicit action potential, or a tissue recruitment volume. Increasing recruitment volume enhances the possibility of body response. Dosimetry of the induced field by the HEMI device is also needed to assess the human health risk associated with such exposure scenarios.

We have identified a set of computational tools to develop an electrical dosimetry model for a HEMI device exposure applied to an idealized physiological geometry while including tissue-specific electromagnetic properties.

2.1. Model Formulation

Finite-Difference Time-Domain Maxwell's Equations Solver

A time-varying electric field, as in the case of a HEMI waveform traveling through a medium, (e.g., human body) will produce a magnetic field which in turn will generate an opposing current (and thus, an electric field). Hence, assessment of the field's potential hinges on the evaluation of the electromagnetic field using Maxwell's equations, which are given in differential form by:

$$\begin{cases} \nabla \cdot \vec{D} = 0 & \text{Gauss's law} \\ \nabla \cdot \vec{B} = 0 & \text{Gauss's law for magnetism} \\ \nabla \times \vec{E} = -\dfrac{\partial \vec{B}}{\partial t} & \text{Maxwell} - \text{Faraday equation} \\ \nabla \times \vec{H} = J + \dfrac{\partial \vec{D}}{\partial t} & \text{Ampere's law} \end{cases} \quad (1)$$

where $\vec{D}$ is the electric displacement field, $\vec{B}$ is the magnetic flux density, $\vec{E}$ is the electric field, $\vec{H}$ is the magnetic field strength, and J is the current density. These equations are solved numerically using a generation source (HEMI device) to determine the electric field, current, and potential (voltage) throughout the human body.

Maxwell's equations describe the propagation of electromagnetic fields in time and space as the result of an excitation source. The equations are a system of partial differential equations that

require advanced computational methods to solve. In the case of a HEMI device applied to humans, we must solve these equations in a large geometry that represents the body and use an excitation source that mimics the HEMI device. Due to the complexity of the problem and the difficulty posed by solving Maxwell's equations, we seek to identify a robust and efficient numerical method that can solve the equations with our specific application. The finite-difference, time-domain method (FDTD) (Yee, 1966) is the most flexible solution method allowing for simulations over a range of frequencies and the ability to model nonlinear dielectric material properties consistent with human tissue.

Several potential open-source numerical tools for implementing the FDTD method of solving Maxwell's equations were identified. We settled on a list of four tools which fit the parameters of our problem and used absorbing boundary conditions, which were necessary in our case. We determined that GMES, Meep, and Angora (https://sourceforge.net/projects/gmes/, https://meep.readthedocs.io/en/latest/, and http://www.angorafdtd.org/) were all suitable to solve the problem. Each offered some utility, but were lacking either in documentation or ease of implementation related to the programming language interface. After some review and evaluation, we identified openEMS (Liebig, Rennings, Held, & Erni, 2013) as the primary candidate for a robust stable solution.

openEMS (http://openems.de/start/index.php) is an FDTD Maxwell's equations solver that offers several features that make it a good choice for use in a HEMI electrical dosimetry model. The model may be run in 3D Cartesian or cylindrical coordinates. The 3D geometry can be meshed within the tool and a graded mesh can be used, which allows for a more efficient computational solution. openEMS allows for absorbing boundary conditions such as the perfectly matched layer (PML) method often used for electromagnetic problems in open geometries (human body surrounded by air). We have the ability to define an irregular excitation source such as the waveform produced by the X26 Taser device and can define dispersive material properties for different tissues based on location and structure. openEMS provides the best code documentation and set of tutorials out of the pool of potential FDTD tools. There is also an active, online user community and an engaged development team. The tool works as a library that is called MATLAB (or Octave) in the Windows operating system. The MATLAB interface should allow for an easier link with our implementations of the neuron excitation and muscle stimulation (SENN and Shorten) models. Electric field and current density results from openEMS can be analyzed, plotted, and visualized within MATLAB or Paraview (a free 3D visualization platform).

Computational Geometry

The first step in the construction of the electrical dosimetry model is to define the computational geometry. We initially used a simple rectangular solid geometrical design to represent the human torso. Dimensions of 40x50x25 cm for the slab represent typical measurements for the adult male torso (NASA, 2018). A padding of 5 cm on each of the 6 sides of the slab was used to represent the air surrounding the body. The PML absorbing boundary condition will be applied in this region of the computational domain to represent the boundless surrounding air. Initially, a 1 cm resolution is used for relatively fast computational solutions (1-2 hours). This resolution results in a complete 105,000 cell geometry (50x60x35 cells) over a total of 10 million time steps.

This initial grid and mesh was expanded to result in a finer resolution. A 5 mm resolution was achieved by doubling the number of cells in each dimension. This finer resolution results in a more computationally intensive simulation with a duration of 25-30 hours on a 4-core, 3.7 GHz PC with 128 MB of RAM. As we move toward more realistic computational geometries, the finer resolution

will be necessary to accurately determine electrical dose in the tissues that are spatially distributed throughout the body.

A graded mesh was used for areas near the HEMI device excitation source. This region of the geometry experiences the most dynamic changes in electromagnetic field over the course of the pulse, and it is important to represent the electric field as accurately as possible with a high resolution. Resolution in this region was reduced to 1 mm and expanded back to 1 cm as the distance from the excitation source increased. The graded mesh was implemented incrementally with a grading ratio of 1.07.

Dispersive Material Properties for Human Tissues

Human and animal tissue behaves differently depending on the frequency of the electromagnetic signal applied to it. There are two complicating factors for dielectric tissue. First, frequency dependence or dispersion causes permittivity[1] to change with changes to the excitation frequency. Second, there may be a delay in response or relaxation as materials experience a lag in response to an electric field. This relaxation will vary among tissues and frequencies. Permittivity and conductivity data in human and animal tissue has been published by Gabriel (1996) as a function of the excitation frequency. Cole-Cole model parameters were estimated (Andreuccetti & Fossi, 2000), and the authors have published an approach to calculate the dielectric tissue properties for any frequency.

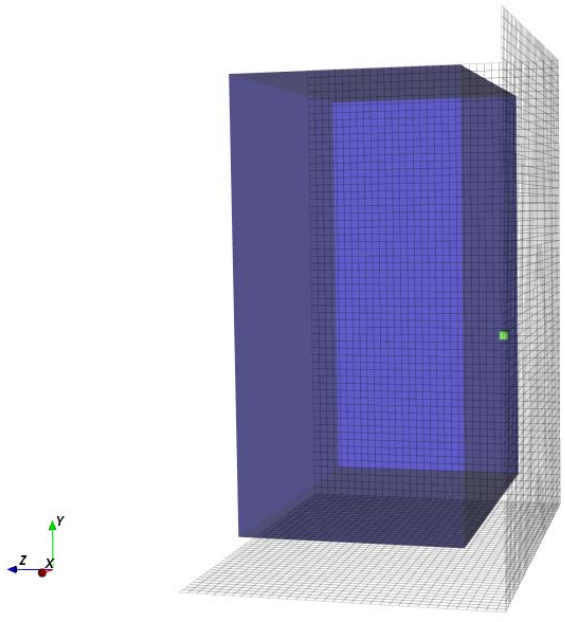

Figure 2. Purple single-material layer of tissue surrounded by air with the excitation source represented by the small green cube.

[1] Permittivity is the ability of a material to store electrical potential energy under the influence of an electric field measured by the ratio of the capacitance of a capacitor with the material as dielectric to its capacitance with vacuum as dielectric.

We have applied a multi-phase approach to modeling the dispersive properties of the different types of human tissue. Model stability was first tested for a single, initial non-dispersive material representing a hypothetical tissue with constant dielectric properties (permittivity and conductivity do not change with frequency) (Figure 2).

Next, to explore the interactions of tissue properties with the model, three regions were defined within the structure with distinct permittivity, conductivity, and density values representing organ tissue surrounded by a layer of bone and further surrounded by a thin layer of skin (Figure 3). This layering approach is a simplified starting point for more accurate layers for skin, body fat, bone, and organ geometries, which will be developed in the future. The location and size of the tissue regions may be precisely defined as input to the electrical dosimetry model.

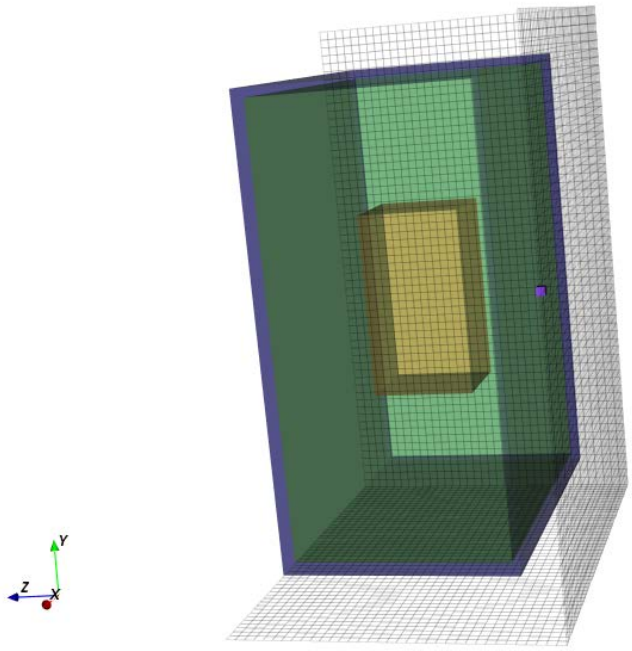

Figure 3. Three layers of tissue modeled (thin purple layer = skin, green layer = bone, yellow layer = unspecified organ).

Model stability was achieved in each case. We then modified the surrounding skin layer by using a simplified Debye model translation of the Cole-Cole parameters to more accurately represent the frequency-dependent dielectric properties (Mustafa, Abbosh, & Nguyen, 2014).

Finally, we implemented a tool in MATLAB to determine the exact predicted permittivity and conductivity of each tissue region based on the complete set of Cole-Cole model parameters found by Gabriel (1996) using the approach of Andreuccetti & Fossi (2000). For a given tissue,

Cole-Cole dielectric model parameters are obtained from a databse and then used to calculate the real and imaginary components of the complex dielectric function. Relative permittivity and conductivity values for the HEMI device-specific waveform frequency can then be obtained from these components:

$$\varepsilon = \varepsilon_0 + \sum_{n=1}^{4} Re\left(\frac{b_n}{1 + (i\omega\tau_n)^{1-d_n}}\right)$$
$$\sigma = \sigma_0 - \omega\varepsilon_0 \sum_{n=1}^{4} Im\left(\frac{b_n}{1 + (i\omega\tau_n)^{1-d_n}}\right) \quad (2)$$

where ε is the relative permittivity, ε_0 is the vacuum permittivity, ω is the angular frequency (a function of the waveform frequency), and b_n, τ_n, and d_n are sets of four Cole-Cole model parameters for the tissue at specific frequencies.

Excitation Source Characterization

The HEMI device excitation source must be defined by location, waveform, direction, and magnitude. The location of the electrodes was chosen to be between 0 and 1 cm depth into the layer of skin. We have initially assumed that a simple Gaussian or sinusoidal waveform represents the excitation pulse. This example waveform will more closely represent the M26 Taser device (Figure 4). The direction of the pulse is assumed to be directly into the torso. Finally, the magnitude of the excitation is about 5.5×10^6 V/m (Singh et al., 2010).

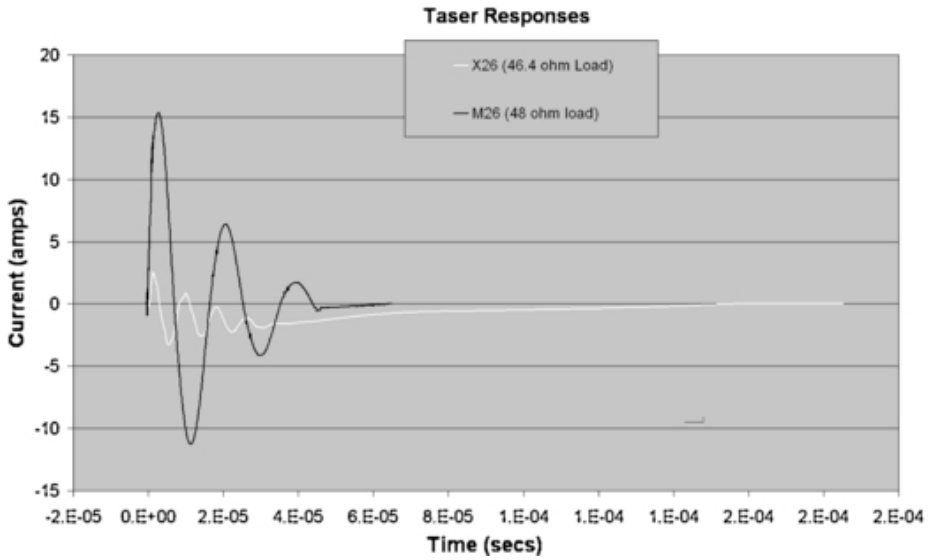

Figure 4. Sinusoidal M26 waveform with approximately 50 kHz frequency given by darker curve.

The FDTD solver has the ability to define an irregular excitation waveform. We have fit a sinusoidal-exponential model to the irregular X26 signal data to determine a functional form for the X26 waveform that may be imported into openEMS (Figure 5). The location and dimensions of the electrodes may be precisely defined in the electrical dosimetry model. Simulations were conducted with either one HEMI device electrode or two electrodes separated by a distance of 14 cm located near the center of the torso. The 1 mm thick electrode darts were assumed to penetrate a distance of 1 cm into the skin tissue layer. The source excitation was simulated over the course of 0.1 to 0.2 ms, capturing the most significant portions of the HEMI waveform.

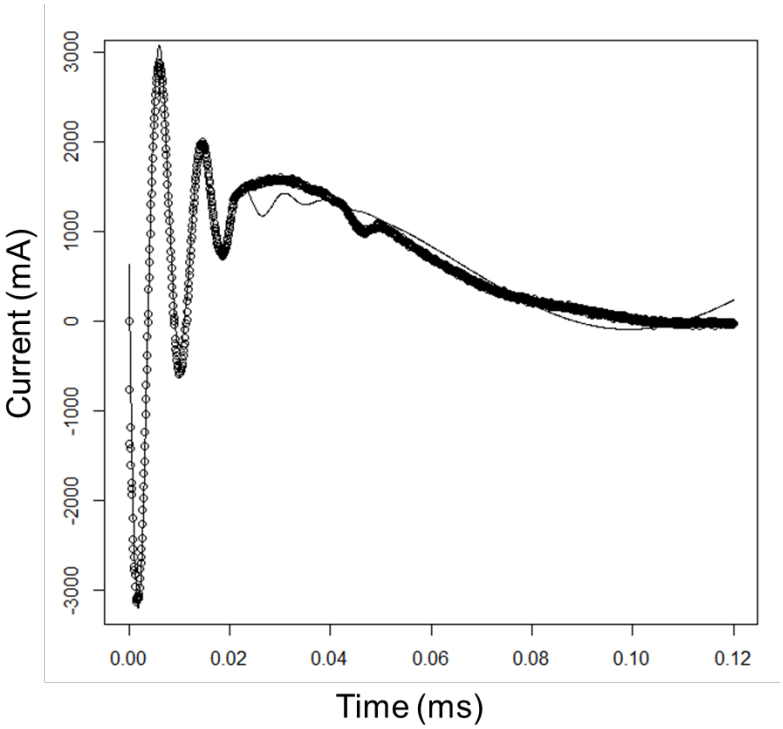

Figure 5. Measured X26 Taser device waveform data (circles) fit with an exponential/sinusoidal function (line).

2.2. Model Predictions

After we defined the 3D computational geometry, boundary conditions, material properties, and excitation source, we were able to use the FDTD solver to simulate the spatial and temporal distribution of the electric field in the human torso. We modified the solver to capture the electric field magnitude and current density at several coronal, sagittal, and axial planes through the torso as a function of time over the course of a single pulse (approximately 0.2 ms).

As expected, we can visualize the periodic fluctuations in the electric field throughout the body with the same frequency as the applied excitation (Figure 6).

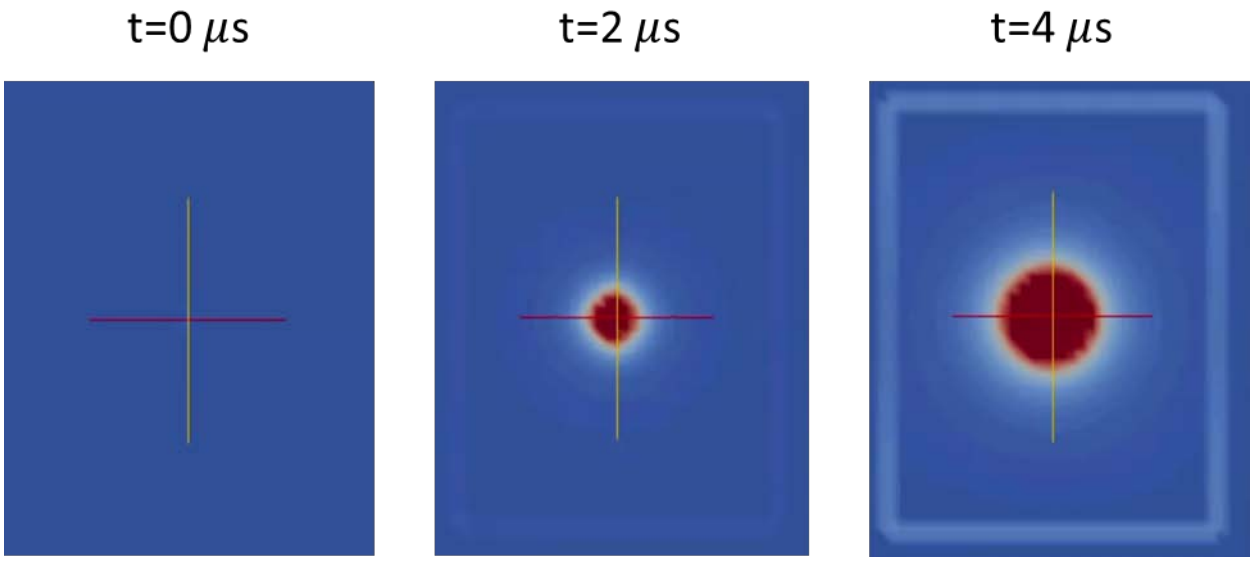

Figure 6. Oscillation in electric field (coronal slice at 5 cm depth) with the excitation source as time increases.

The electric field is observed to decrease in magnitude as you increase the distance away from the source (Figure 7).

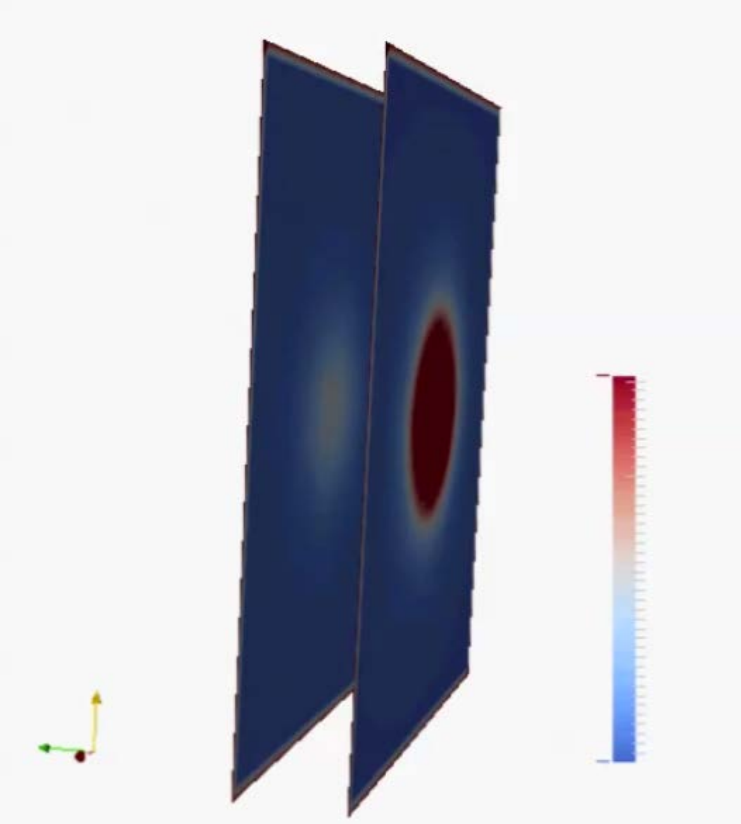

Figure 7. With the excitation source to the right of the figure, electric field is shown to decrease in magnitude as the distance increases away from the source (coronal slices at depths of 5 cm and 10 cm).

When a tissue with high permittivity is added to the geometry, the electric field has difficulty penetrating deeper into that tissue – thus moving around and into surrounding low permittivity tissue instead (Figure 8). In this case, the skin, fat, muscle, and stomach layers have relative permittivity values (compared to vacuum permittivity) of 1116, 91.9, 7648, and 2736, respectively. The electric field moves more easily through the low permittivity fat tissue layer compared to the higher permittivity stomach and muscle layers.

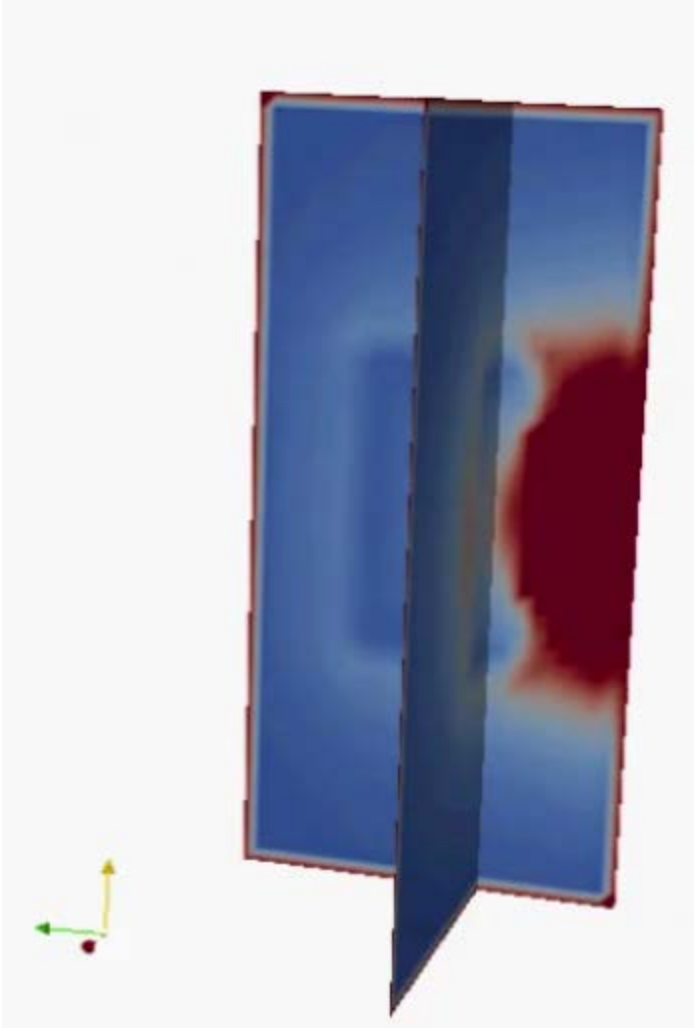

Figure 8. The electric field does not penetrate as much into the tissue with high permittivity located in the center of the geometry (sagittal slice through center of geometry and coronal slice at a depth of 15 cm).

The full 3D electric field or current density can be captured by the FDTD solver allowing for the computation of recruitment volumes based on current density thresholds (Figure 9). Voltage probes can also be placed throughout the geometry which integrate the electric field to determine potential at a specific location. The output can then be used to calculate external neuron voltages that will be used by the motor neuron excitation model.

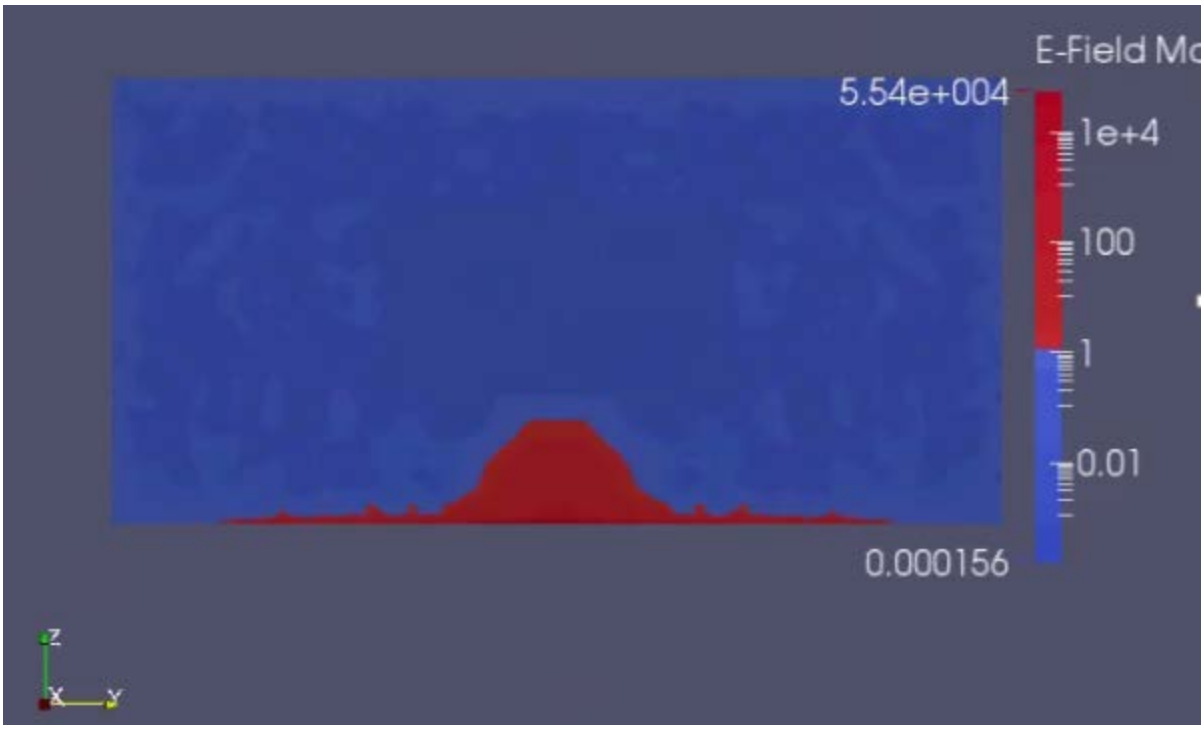

Figure 9. Two-dimensional representation of a recruitment volume calculation at t = 0.02 ms in a cross-section of the geometry.

We have generated stable solutions of Maxwell's equations using the FDTD method in a simplified model of a HEMI device interacting with an idealized human torso. The dosimetry model calculates the 3D electric field as a function of time throughout the torso geometry. This can be translated into recruitment volumes and interfaced with the neuron excitation (SENN) model to determine internal neuron voltages and action potentials based on time post-exposure and the location of the nerve.

2.3. Future Model Development

To accurately estimate the electrical dose in a person after a HEMI exposure under different use scenarios, additional complexity and accuracy must be integrated into the model. Model stability must be confirmed at each step of the process. Once the tissue and source models can sufficiently capture the specific properties of human tissue and HEMI devices, we will begin to test adding complexity to the computational geometry. Future plans include increasing the resolution of the grid and adding additional PML cells (air boundary). The mesh must be refined and graded such that resolution is increased potentially up to 1 mm resolution. We will also explore the use of a cylindrical model of the human torso and the possibility of eventually incorporating an anatomically accurate virtual human geometry that has been made publicly available (Christ et al., 2009; Massey & Yilmaz, 2016).

Improvement of the generalized model is necessary on several fronts. To leverage available animal data, a swine geometry must be developed that includes species-specific tissue distribution and location. We will investigate the effect of variations in tissue distribution, size, and other physiological parameters on electrical dose metrics. It may also be necessary to modify the Cole-Cole model implementation to better capture the effect of current sources which exhibit a

wider bandwidth of excitation frequencies. The generalized model must also be adapted to more accurately reflect the human body by including additional tissue layers and improving the spatial accuracy and distribution of these issue layers. Finally, we will investigate the effect of HEMI device electrode location, penetration, and gap width on electrical dosimetry predictions.

3. Motor Neuron Excitation

The electric field from a HEMI device penetrates nerve fibers and triggers muscle action. The muscle response is related to the potential generated across and within the nerve cell and depends on several parameters such as the source waveform and its intensity (electrical dosimetry), positioning of the HEMI device probes, and dimensions of the cells and their distance from the probes. A cell excitation (Spatially Extended Nonlinear Network or SENN) model (McNeal, 1976; Reilly & Diamant, 2011) is used to compute threshold current and action potential. A short review is provided on the theory behind the electric field generated within the cell and signal reaching the muscle, which will be used in the next section to compute muscle response. The theoretical model will be used to assess the required strength of the HEMI device output for generating action potential, and inspecting various parameters discussed above on which action potential and muscle response depends. This information will aid in the evaluation of existing and potential HEMI devices for health and risk outcomes.

3.1. Model Formulation

The HEMI device applies a current that travels through the body and generates an electric field. The field strength external to a nerve cell membrane must be evaluated to determine transmembrane, cell internal, and action potentials. Ideally, the solution to the set of Maxwell's equations is needed to calculate the electric field (discussed in Section 2). However, the complexity of the physics and lack of a realistic geometry of the human body hampers a detailed 3D modeling approach. Instead, we assumed a 1D model of an isolated nerve cell lying on the same plane as the electrodes of the HEMI device. The electric fields were calculated for two scenarios: the electrodes touching the surface of the body and the electrodes penetrating the skin. The external potential, V, (i.e., potential outside of a cell membrane) is given by

$$\begin{cases} V = \dfrac{I\rho}{2a\pi r}; & \text{Point source} \\ V = \dfrac{I\rho}{2a\pi L} Ln\dfrac{r}{y}; & \text{Wire electrode} \end{cases} \tag{3}$$

where ρ , L , r, and y are the body resistivity, length of the axon, distance of the electrodes from the center of the fiber nerve, and distance of a node from the center of an axon, respectively. Constant a is 1 when the electrodes touch the surface of the body and 2 when the electrodes penetrate the skin. The set of equations (3) provide an ideal scenario for quick calculation of the external potential field.

A nerve cell may be visualized by a long chain of a fiber nerve (Figure 10A). Electric current crosses the cell membrane through the gaps between myelinated fibers (nodes of Ranvier). The difference between the external and internal potential across the cell membrane gives rise to transmembrane current, which occurs due to voltage and ion concentration differences across the membrane. A network model presented in Figure 10B can be used to predict the

transmembrane and action potentials. The single-path ionic pathway in this figure represents several pathways for different ions such as *Na*+ and *K*+.

The current flowing from the ionic and voltage pathways into a nodal point (Figure 10B) is balanced by the outgoing current through the axon. The following relationship is obtained by converting the currents to potentials.

$$\frac{dV_n}{dt} = \frac{1}{C_m}\left[G_m\left(V_{\mathrm{n}-1} - 2V_{\mathrm{n}} + V_{\mathrm{n}+1} + V_{e,\mathrm{n}-1} - 2V_{\mathrm{e,n}} + V_{\mathrm{e,n}+1}\right) - I_{i,n}\right] \quad (4)$$

where $I_{i,n}$ is the net ionic current, C_m is the membrane capacitance, G_m is the conductance of the membrane, and $V_n = V_{i,n} - V_{e,n}$ is the transmembrane voltage, in which $V_{i,n}$ and $V_{e,n}$ are internal and external potentials, respectively. A nerve fiber of length 100 times its diameter (0.2 cm) was divided into 51 nodes and an equation (4) was developed for each node. The set of 51 equations and 51 unknowns were solved simultaneously to determine transmembrane potential difference across the nerve cell at different nodes. The selected number of 51 nodes was sufficient for model simulations. No improved accuracy was obtained by increasing the number of nodes beyond 51.

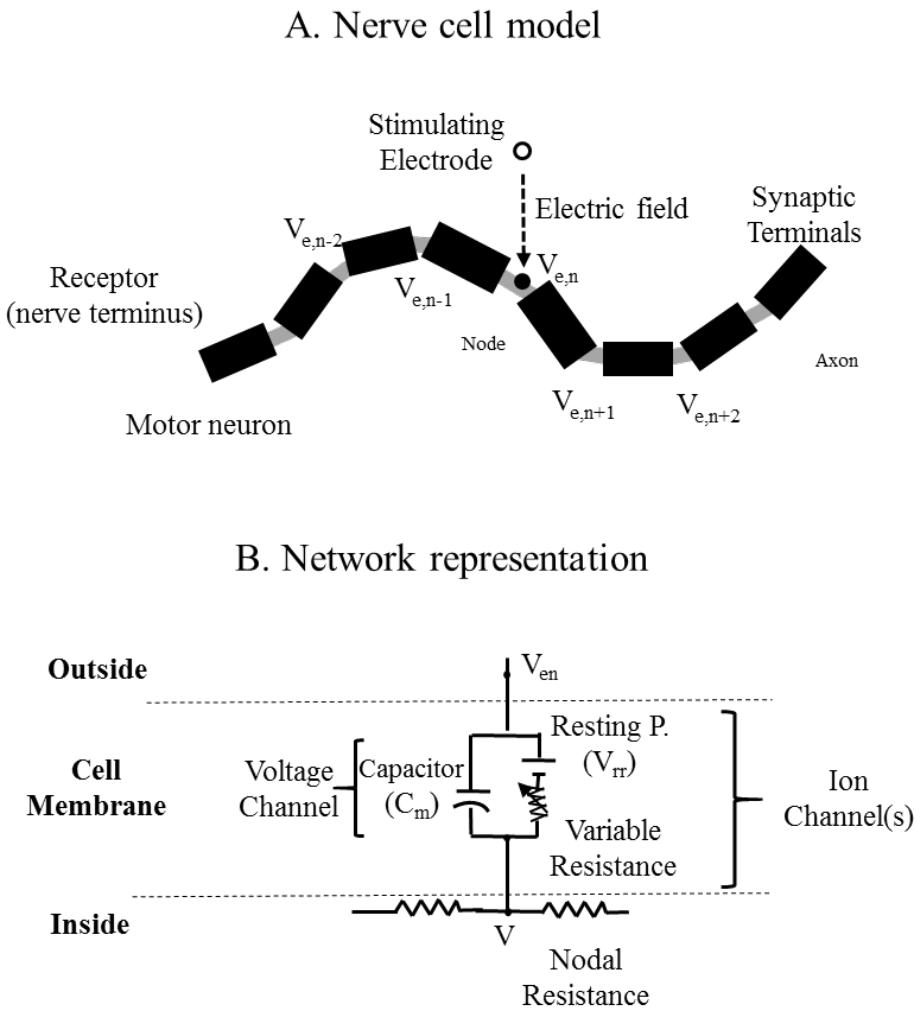

Figure 10. Diagram of a nerve cell for modeling action potentials

Two major computations were made: calculations of the threshold current from the HEMI device and transmembrane potential across the cell at the threshold value for various device and nerve cell parameters. The analysis aids in evaluating specific device designs and use cases and in the estimation of action potentials that may be fed into the muscle response model for health risk assessment.

3.2. Model Predictions

HEMI devices generate pulses of different magnitudes and waveforms. In this task, we aim to estimate the resulting action potentials that result from exposure to different HEMI devices and under different use case scenarios. Figure 11 shows a typical waveform generated by a HEMI device assuming the two electrodes are far apart. The SENN model was utilized to predict the threshold current for the device. The device waveform in Figure 11 has several peaks. The threshold current is the amplitude of the highest (first) peak that leads to an action potential within the fiber nerve. It was assumed that action potential was generated when the transmembrane potential exceeded 80 mV. Model simulations were conducted for a $20\ \mu m$ type A nerve fiber with gap width of $2.5\ \mu m$, axoplasm resistivity of $110\ ohm - cm$, and tissue resistance of $300\ ohm$,

when the device was 1 cm from the nerve cell. Model predictions resulted in a threshold amplitude of 36 mA and 28.5 mA when the electrode either touched the surface of the body or penetrated the skin by a distance of about 0.85 cm, respectively. Thus, a small current was required to induce muscle response. The amplitude of the current was smaller when the electrodes penetrated the skin. The magnitude of the current increases when the probe is farther away from the cell. Hence, while adequate for gaining insight and acquiring general information, single-cell analysis is insufficient to determine the magnitude of the minimum required (threshold) output current of the device. The threshold current should be computed for all nerve cells of the torso to determine the (recruitment) volume of tissues when the potential across the cell membrane exceeds 80 mV. Muscle action is related to recruitment volume.

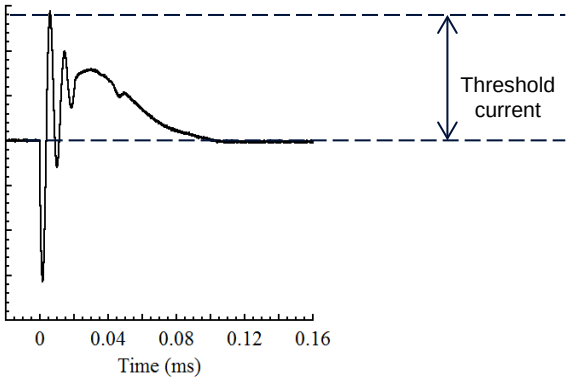

Figure 11. A typical waveform produced by a HEMI device.

The transmembrane potential (voltage) across a nerve cell membrane at several nodes of a nerve cell is given in Figure 12 when the electrode is touching the body surface. Calculations included 51 nodes directly below the electrode for the 1.6 millisecond duration of the waveform. Figure 12 shows model predictions for the first 10 closest nodes to the electrodes. The thick line in the figure corresponds to the node directly below the electrode (i.e., the closest node to the HEMI device), which was the first node to be excited. The shapes of the potential curves were similar among all nodes, but different from that of the pulse (Figure 11) despite following the general rise and fall pattern. Transmembrane potential increased rapidly to reach a maximum value of about 40% higher than the required 80mV transmembrane potential, and dropped gradually to zero by the end of the 1.6-ms source excitation period. The response (delay) time of a node to the current from the device was directly related to the distance of the node from the HEMI source. Transmembrane potential (and thus action potential) was present only during the period of applied pulse.

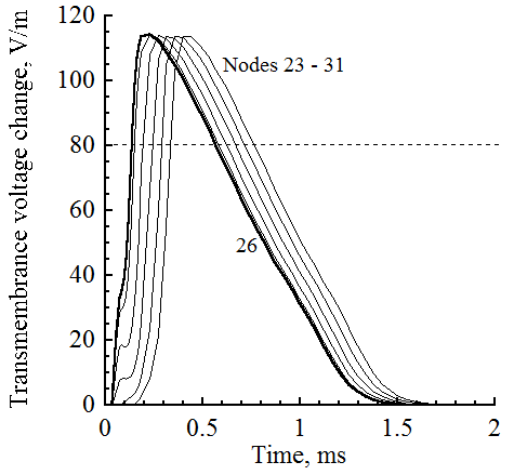

Figure 12. Action potential generated in several nodes of a nerve fiber.

To study the significance of the threshold current, the same calculations were made when the source output current was 80% and 120% of the threshold current. Model predictions are provided in Figure 13. Transmembrane potential only reached 25% of the required 80 mV to generate an action potential (left panel) for the first excited node (26) when the HEMI source emitted 80% threshold current. The current transmitted through other nodes was exceedingly small as the nodes moved away from the HEMI source. Thus, no action potential could have been generated below the threshold current. The right panel in Figure 13 provides the results when the HEMI output current is 120% of the threshold current. Results were very similar to those in Figure 12 both in terms of the magnitude and shape of the curves. Thus, a similar action potential was expected.

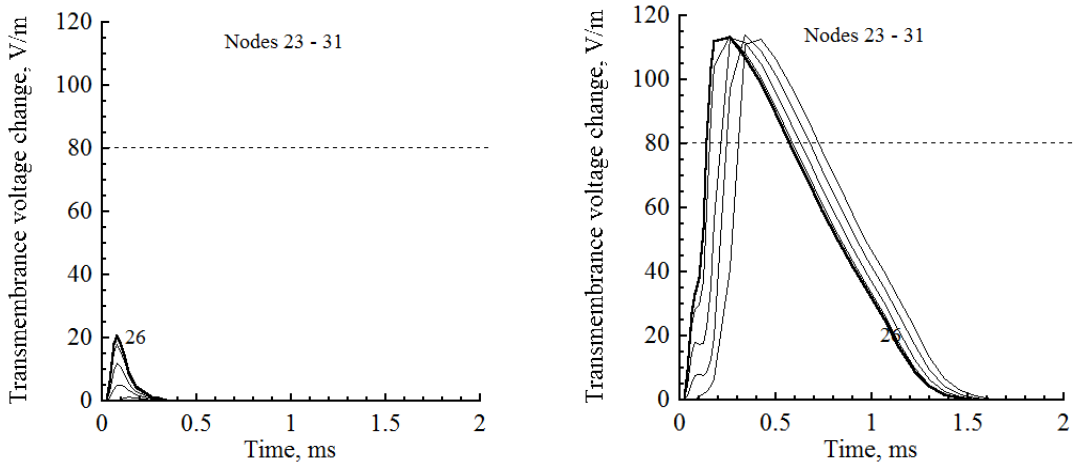

Figure 13. Transmembrane voltage at 80% (left panel) and 120% (right panel) of the threshold current for 10 nodes directly below the HEMI source.

A more clear visualization of the trend can be made if Figure 12 and Figure 13 are combined for the first excited node as shown in Figure 14. Transmembrane voltage fell far short of the required voltage for action potential for sub-threshold currents. There appeared to be only a minimal increase in transmembrane potential when threshold current increased above the

threshold value. Thus, no gain in action potential would be expected. Increasing the current of HEMI device output will increase the likelihood of adverse health outcome. Hence, threshold current appears to be the desired current to elicit action potential with least possibility of inflicting adverse health outcome.

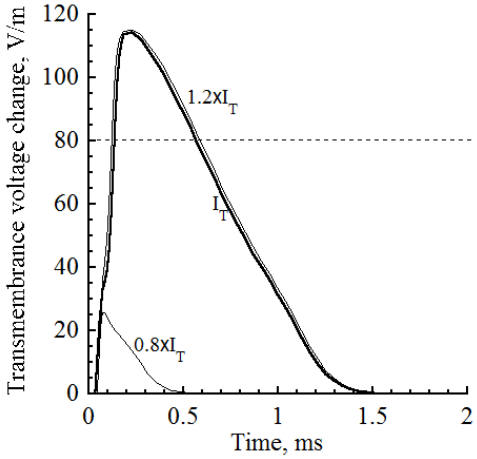

Figure 14. Transmembrane potential across the first excited node of a nerve cell for device currents of 80%, 100%, and 120% of the threshold current.

The peak transmembrane potentials were similar among different nodes (Figure 12). Figure 14 included only one current output above and below the threshold current. To study the generality of the conclusion made above, peak transmembrane potential was calculated at different HEMI device output currents ranging from 0 to 200% above the threshold current (Figure 15). Distinct behavior emerged for the peak threshold current. The peak potential increased slightly when the device output current was below the threshold current. The peak potential rose sharply when the device current reached near the threshold current. The peak potential remained relatively constant for output currents at and above the threshold current. This finding emphasizes the conclusion above that threshold current is the optimal value for the device to bring about the desired muscle response while minimizing the likelihood of adverse health outcomes. However, the threshold current depends on the distance of the nerve cell from the device, and therefore, must be calculated at different distances to determine the recruitment volume (volume of tissues with threshold current above that necessary to elicit action potential).

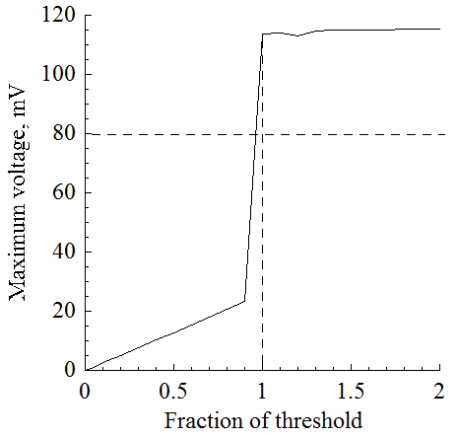

Figure 15. Maximum potential in the axon as a function of current outputs of the device.

Figure 11 – Figure 15 were computed based on the assumption that at least 80 mV of transmembrane potential was required across the cell membrane to generate action potential. This value of transmembrane potential is compatible with the resting potential, which is typically about 60 to 70 mV. To inspect the sensitivity of the action potential with respect to the predefined requirement for transmembrane potential, the threshold current was reevaluated for different voltage requirements for transmembrane potential (Figure 16). The threshold current increased sharply with increasing transmembrane potential below 20 mV. The threshold current remained constant with increasing transmembrane potential between 20 mV and 110 mV, and rose sharply thereafter. Thus, an action potential is insensitive to the required transmembrane potential for action potential as long as transmembrane potential does not deviate from about ±40% of the resting potential.

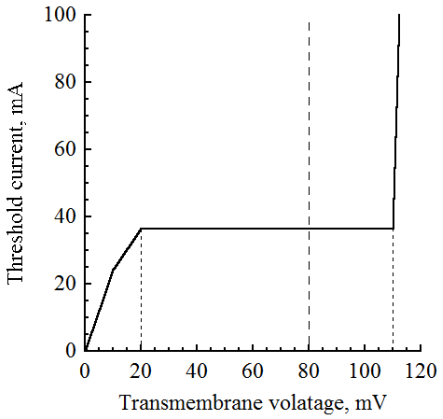

Figure 16. Variation of threshold current with changes in the required transmembrane potential required to generate an action potential.

Threshold current varies with the distance between electrodes. To investigate the influence of electrode displacement on threshold current, different distances between the electrodes were assumed and the threshold current was calculated using the same nerve cell and tissue properties stated above. Model predictions are given in Figure 17. Nerve cells did not experience an electric field when the two electrodes were touching. Current from one electrode traveled directly to the other and did not distribute throughout the body. The threshold current dropped sharply as the

distance between the two electrodes increased and reached a minimum current when the two electrodes were about 1.5 cm distance apart. The threshold current increased slightly with additional increase in distance and approached a plateau. Therefore, there was an optimal distance between the two electrodes to generate the minimum threshold current to induce action potential. However, larger distances between electrodes above the optimal distance resulted only in a slight increase in the threshold current. Threshold current is nearly constant for an electrode distance of 1 cm or greater.

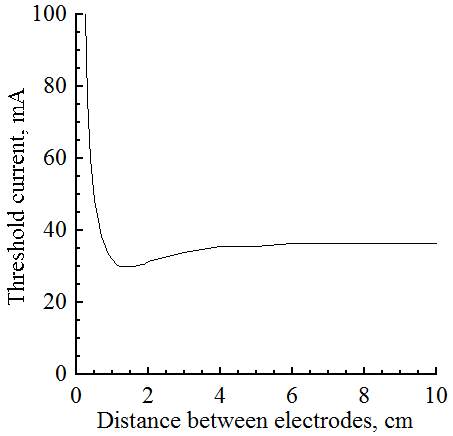

Figure 17. Variation of threshold current with distance between electrodes for a nerve cell 1 cm from the electrodes.

Threshold current changes with the distance of the nerve cell from the two electrodes. Figure 18 gives model predictions for the threshold current as a function of the nerve cell distance from the electrodes. The threshold was very small and negligible (i.e. any current would have resulted in muscle action) when one (cathode) electrode was within 1 cm of the nerve cell. Threshold current increased sharply as the nerve cell's location increased farther from the electrode. This finding implies that either the recruitment volume should encompass the entire torso or the HEMI source needs to be near the nerve cell to generate action potential.

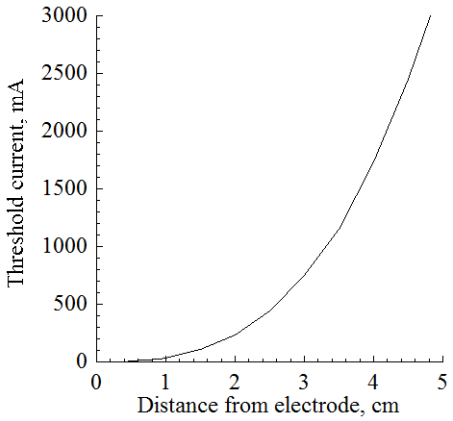

Figure 18. Changes in threshold current with varying distance of the nerve cell from the HEMI source.

The generated action potential and current through the nerve cell at the threshold current of the device is given in Figure 19. The pattern for potential and current change over time was similar to

that of transmembrane potential (Figure 12); however, the values were much smaller. The generated current was in mA while the potential was around 1 V. Action potential existed only for the duration of the current applied by the device. This finding provides guidance for input potential or current to muscle excitation models to predict muscle response and possible health adverse outcomes.

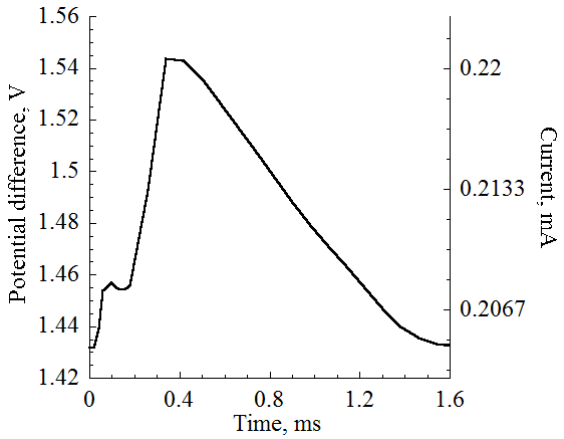

Figure 19. Inter-nodal potential and current in a nerve cell.

The above analysis is based on a single waveform (Figure 11). There is an interest in HEMI devices that deliver longer durations or repeated waveforms with and without pause between pulses. Longer and repeated pulses may increase effectiveness and risk of adverse health outcome unless the threshold current is reduced. The bar plot in Figure 20 gives the predicted threshold current as a function of the number of pulses from the HEMI device. There was no time gap between pulses. The threshold current decreased when increasing the number of pulses. Results also indicated that there appeared to be an optimal number of pulses above which no reduction of threshold current could be achieved. The number of pulses is estimated to be about 6 or 7 or about 10 ms based on the trend of the threshold curve in Figure 20. However, additional studies are needed to determine the most effective waveform and duration that yields the lowest threshold current.

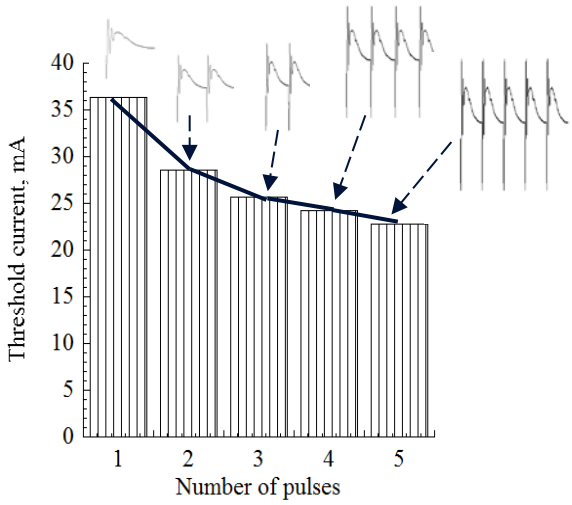

Figure 20. Threshold current for different number of waveforms.

The results presented in Figure 12 – Figure 20 are for the case of electrodes touching the surface of the body. The threshold current was slightly lower when the electrodes penetrated the skin (Figure 11). Model prediction and conclusions using threshold current for electrodes penetrating the skin were almost identical to results presented above. Thus, they are not repeated in this report.

4. Muscle Excitation-Contraction Model

The processes involved in the physiological response to an electrical dose initiated by a HEMI device are dynamic and complex. Furthermore, these dynamics can be affected by genetic disposition, pre-existing medical conditions, or the physiological state of an exposed individual. To capture these complexities, we are developing a mathematical model of muscle cell excitation-contraction resulting from extracellular electrostimulation. We have identified the Shorten model (Shorten, O'Callaghan, Davidson, & Soboleva, 2007) for this purpose, which we will adapt and modify as necessary. The model can be used to estimate the damage of a muscle fiber exposed to excessive electrical stimulation, and the predictions of the model will be used as inputs for clinical risk assessment.

4.1. Model Formulation

The Shorten model is a system of four connected ODE models: 1.) the muscle membrane electrophysiology model represents the dynamics of a muscle fiber membrane action potential; 2.) the calcium dynamics model describes the transport of calcium stores between the sarcoplasmic reticulum and the intracellular region in response to an action potential; 3.) the crossbridge dynamics model represents the mechanics of muscle contractions in response to intracellular calcium influx; and 4.) the phosphate dynamics model describes negative feedback in the system via inhibition of calcium release. Diagrams of the four model components are provided in Figure 21-Figure 24.

The muscle membrane model (Figure 21) describes the time-dependent flux of sodium, potassium, and chloride ions across the sarcolemma and t-tubules of the skeletal muscle fiber. The process can be stimulated by administering an action potential triggered from a motor neuron. This causes a rapid influx of sodium ions into the interstitial space followed by an extrusion of potassium ions. This process depolarizes the muscle cell membrane, which then triggers calcium ions (Ca^{2+}) in the sarcoplasmic reticulum (SR) to be released into the myoplasm.

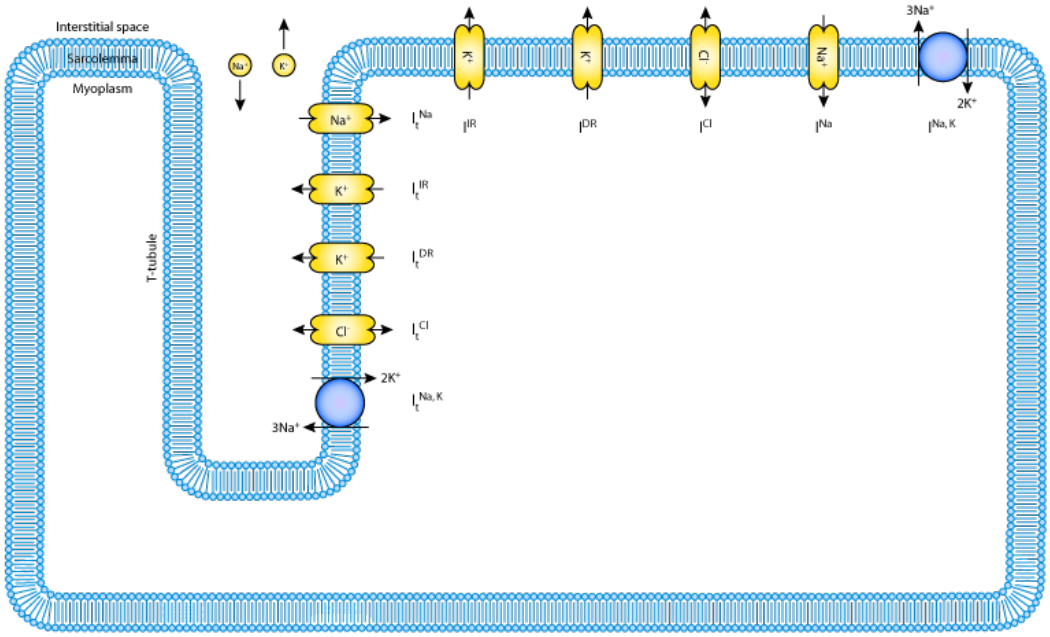

Figure 21. The muscle membrane electrophysiology model (Shorten et al., 2007).

The calcium dynamics component of the Shorten model describes the transport of calcium ions between the SR and the myoplasm of the muscle fiber (Figure 22). Following an action potential, activated ryanodine receptor (RyR) complexes allow for Ca^{2+} to be released from the SR into the myoplasm, where they initiate muscle contractions by binding to troponin. Parvalbumin and ATP are mobile and immobile buffers, respectively, that bind to Ca^{2+}, and calsequestrin binds to Ca^{2+} when it is transported back into the SR.

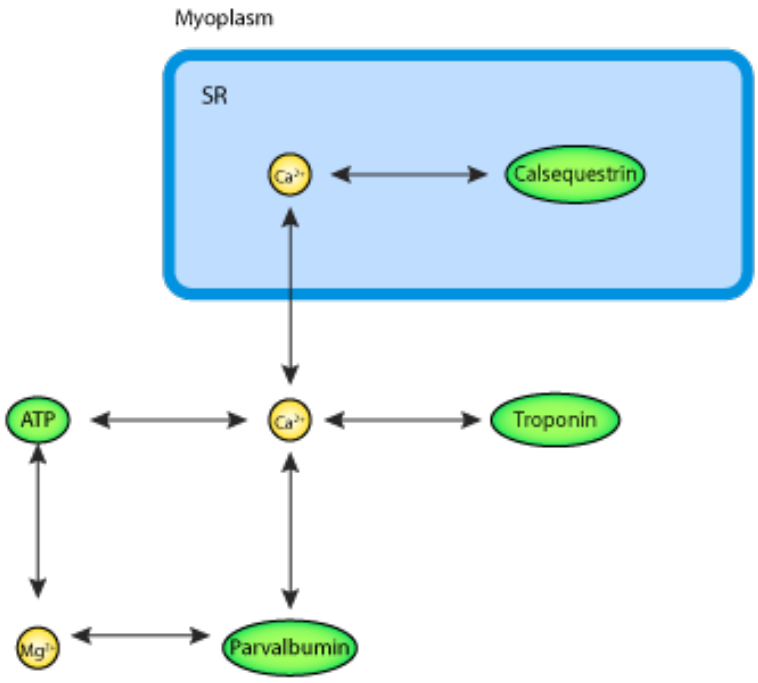

Figure 22. The calcium dynamics model (Shorten et al., 2007).

When two calcium ions bind to troponin in the myofibrils of a muscle cell, a complex series of mechanical steps, referred to as crossbridge (XB) dynamics, allow thick and thin filaments to attach and generate force through a mechanism known as a power stroke. This results in the contraction of the myofibril sarcomeres that are responsible for muscle contractions. A diagram of the XB dynamics component of the Shorten model is provided in Figure 23.

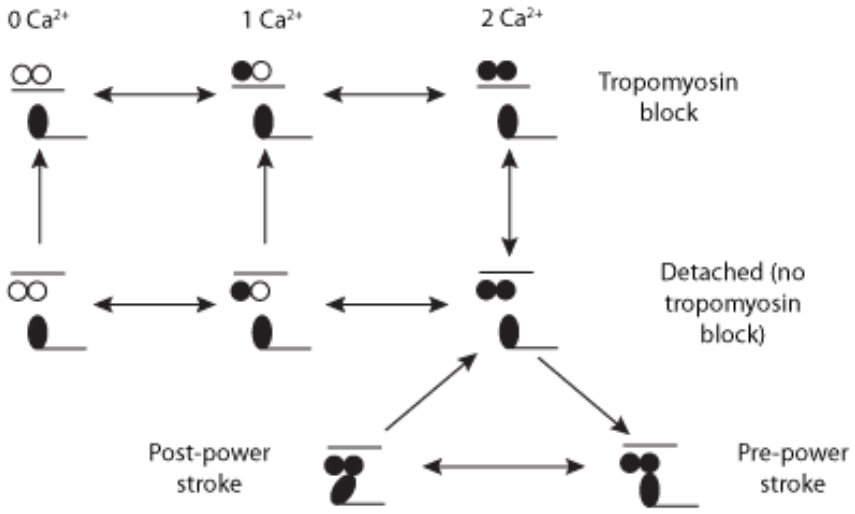

Figure 23. The crossbridge dynamics model (Shorten et al., 2007).

The Shorten model was developed to study muscle fatigue, which is a product of skeletal muscle cell overstimulation. This phenomenon was integrated in the Shorten model via inorganic phosphate, which is assumed to build up in the myoplasm after extended periods of muscle stimulation and inhibit subsequent calcium buildup and muscle contractions (Figure 24). The phosphate dynamics provide a negative feedback in the model that prevents excessive force generation in the sarcomere.

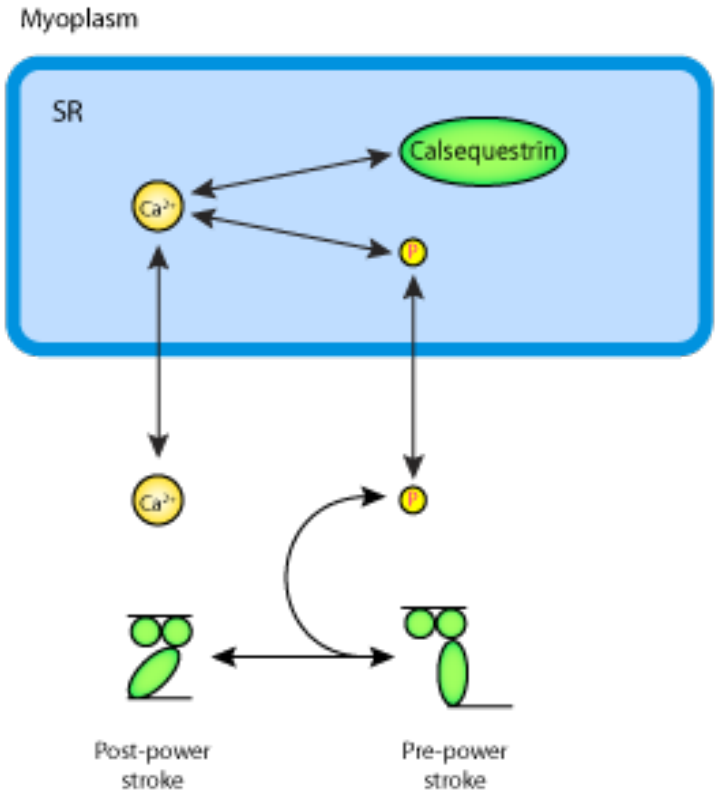

Figure 24. The phosphate dynamics model.

4.2. Model Predictions

Code for the Shorten model has been made publicly available in the following formats: C++, Fortran, MATLAB, and Python. In its available format, the code only contains parameter values for the extensor digitorum longus (EDL), a fast twitch muscle fiber, although parameter values have also been established for the soleus (SOL), a slow twitch muscle fiber. The code also contains the parameters and ODE equations necessary to run the model. We have expanded the Python code to run basic analysis of the model, and we have developed a technical reference that links the mathematical equations with the sub-models of Shorten's excitation-contraction model. This technical reference will be extended as components are added to the model.

After adapting and expanding the Python code of the Shorten model, a simple verification test was administered to ensure model preservation. Figure 25 reproduces a simple application of the model exposed to a single electrical pulse at 15 ms (reproduces Figure 5 from Shorten et al. (2007)).

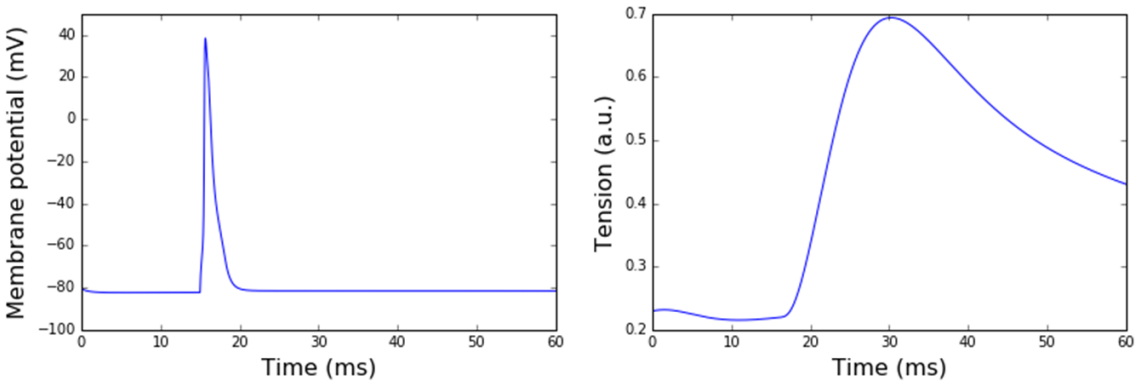

Figure 25. Verification of a muscle twitch using the Shorten model.

Next, the response of the model to three different pulse trains was simulated. The pulse trains are defined as a series of half-millisecond, 150 μA/cm^2 stimulants, evenly spaced over time, with 20, 50 and 100 Hz frequencies (Figure 26). In reality, electric stimulation transferred from motor neurons to the muscle fiber sarcolemma will have a much more complex waveform. When integrating the excitation-contraction model in the full HEMI modeling system, a physiologically accurate current density function will be estimated and applied to the excitation-contraction model.

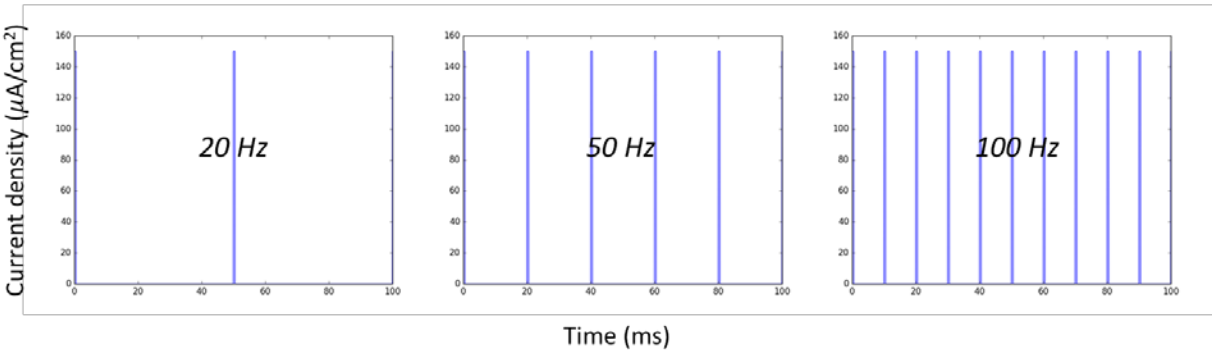

Figure 26. Pulse trains in three frequencies used to test the Shorten model.

The Shorten model was run with each of the three pulse trains mentioned above for 100 ms, and sample outputs are provided in Figure 27. This provides a snapshot of the large amount of molecular information estimated by the model. Ca^{2+}, membrane potential and tension are provided because these parameters may be useful in developing a relationship of model predictions to risk of cellular damage.

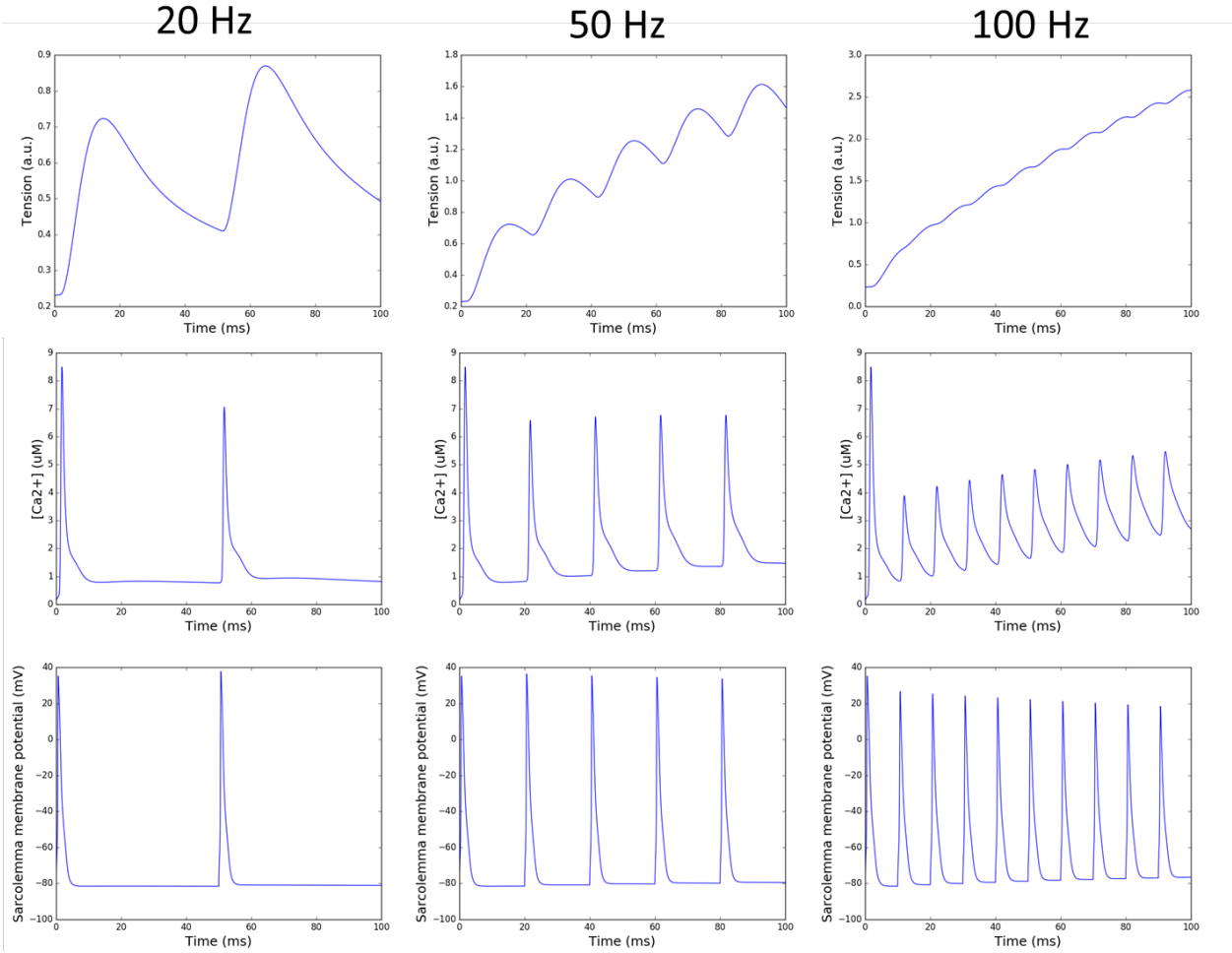

Figure 27. Sample simulations of the Shorten model in response to 20, 50, and 100 Hz pulse trains: Muscle fiber tension (top), free Ca^{2+} in the myoplasm (middle), and sarcolemma membrane potential (bottom) are provided.

In addition to testing the Shorten model, we have conducted a basic sensitivity analysis of model variables likely to be related to muscle damage. For example, we have determined the dependence of the maximum tension on pulse trains with varying frequency and pulse length (Figure 28). Similarly, we have evaluated the dependence of myoplasmic calcium when varying pulse train characteristics (Figure 29). Interestingly, the maximum calcium is threshold-dependent on the frequency for each pulse length. These dependencies are important to understand before determining the sensitivity of the model to realistic pulse waves stimulated by motor neurons, which may vary greatly between HEMI devices.

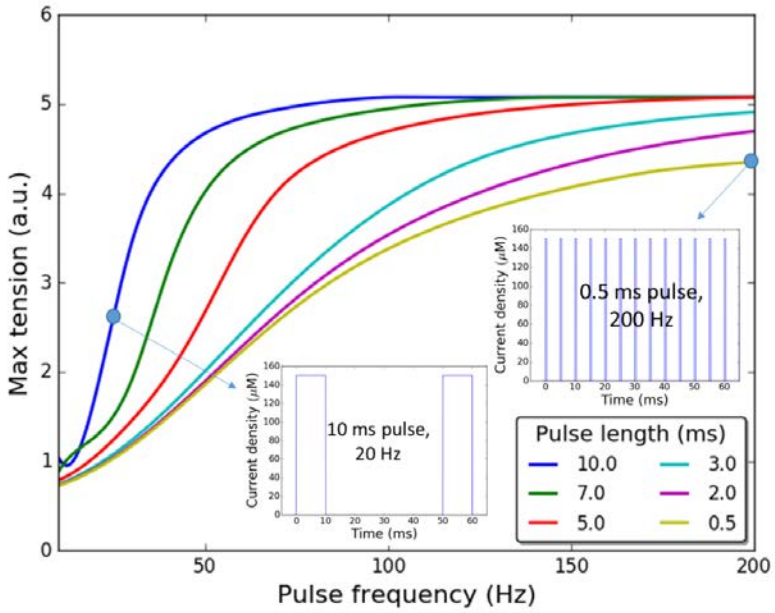

Figure 28. Muscle fiber tension of the Shorten model dependent on pulse length and frequency. Electrical current densities were applied for 1 second and maximum tension was measured by the number of attached crossbridges, post-power stroke.

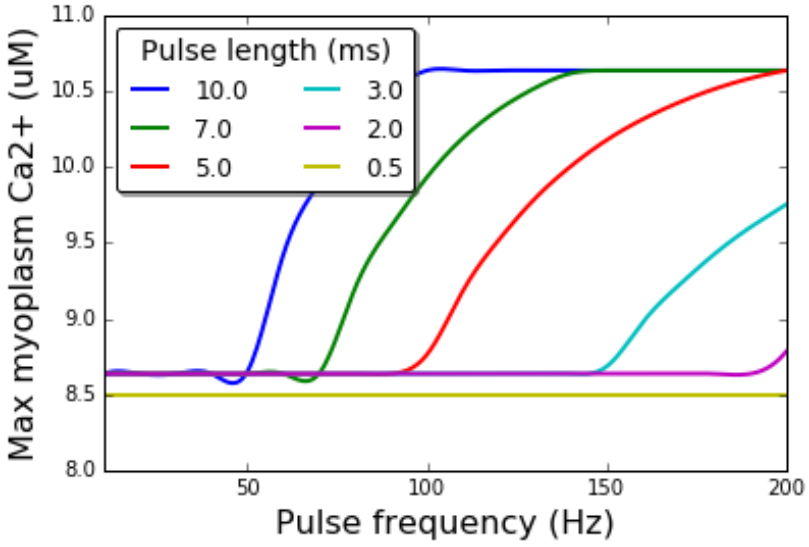

Figure 29. Myoplasmic calcium of the Shorten model dependent on pulse length and frequency. Electrical current densities were applied for 1 second and maximum Ca^{2+} was estimated.

4.3. Future Model Development

In its current form, the Shorten model is unable to produce some of the physiological processes that have been directly implicated in rhabdomyolysis. Furthermore, the model was built under certain assumptions to reduce model complexity that may limit model predictability. Before using the Shorten model for simulating excitation-contraction dynamics, we will evaluate how the following three model limitations will be addressed: 1. the model does not account for ATP depletion, 2. the model only accounts for two muscle fiber types, and 3. the geometry simulated by the model only represents a half-sarcomere. Specific ideas for addressing each of these model limitations are provided below.

Extended electrical stimulation of muscle cells can result in massive energy usage in the form of ATP hydrolysis. Because PCr acts as a buffer for ATP, ATP does not deplete for light to moderate stimulation (Hultman & Sjoholm, 1983). However, at much higher levels of stimulation, ATP will deplete when PCr is unable to keep up with demand (Bergstrom & Hultman, 1988; Karatzaferi, de Haan, Ferguson, van Mechelen, & Sargeant, 2001; Soderlund & Hultman, 1991). ATP depletion can cause dysregulation of ion pumps, which rely on the hydrolysis of ATP for energy. This can result in a series of adverse responses including an upregulation of sodium (Torres, Helmstetter, Kaye, & Kaye, 2015) and unsuppressed calcium buildup in the myoplasm (Kim et al., 2016). As long as calcium is abundant in the myoplasm, XBs will continually form, and as ATP is depleted, the XB formations will not be able to detach (Brumback, Feeback, & Leech, 1995; Criddle, 2003; Moghtader, Brady, & Bonadio, 1997; Russell, 2000; Visweswaran & Guntupalli, 1999). This can result in extended periods of intense muscle contractions that can damage muscle fibers (Huerta-Alardin, Varon, & Marik, 2005; Kim et al., 2016; Torres et al., 2015; Wrogemann & Pena, 1976). In fact, a highly stimulated membrane potential can cause Ca^{2+} extrusion pumps to operate in reverse, pumping more calcium into the myoplasm (Gissel, 2005; Kim et al., 2016; Zhang, 2012). ATP depletion and calcium dysregulation have been correlated with rhabdomyolysis (Gissel, 2005; Kim et al., 2016; Zhang, 2012).

Many processes that are modeled by the Shorten model require ATP, including ion pump dynamics and XB cycling. However, the Shorten model assumes that there is an infinite supply of ATP available for these processes. Mechanistic models of the PCr circuit have been developed (Arsac, Thiaudiere, Diolez, & Gerville-Reache, 2004; Chance et al., 1985; Nevill, Jones, McIntyre, Bogdanis, & Nevill, 1997), and we will evaluate the prospect of integrating these models with the Shorten model. This would allow the model to accurately reproduce ATP depletion in extreme muscle stimulation conditions.

Although the Shorten model captures a large amount of detail at the molecular level, several assumptions have been made that could potentially have an impact when using the model to predict rhabdomyolysis. For instance, the model is only parameterized for extreme muscle fibers (fast and slow twitch), but does not account for the muscle types that lie within this range. A recent study has developed and validated parameters for the Shorten model that mimic the entire range of muscle types (Röhrle, Neumann, & Heidlauf, 2016). If deemed necessary, the model extension discussed in Röhrle et al. (2016) could be leveraged when advancing the fidelity of the excitation-contraction model.

An additional limitation of the Shorten model is that it only captures the dynamics of a single muscle fiber. To address this limitation, several studies have developed multiscale models of muscle dynamics by integrating the Shorten model with complex muscle geometries (Mordhorst, Heidlauf, & Röhrle, 2015; Rohrle, Davidson, & Pullan, 2012). We will evaluate the results of these studies and leverage any modeling capabilities necessary.

4.4. Predicting risk from excitation-contraction dynamics

After establishing and validating an excitation-contraction model, components of the model will be used to estimate risk of serious injury such as rhabdomyolysis. The most informative clinical biomarkers of rhabdomyolysis are plasma levels of creatine kinase (CK), potassium, and myoglobin (Brumback et al., 1995; Criddle, 2003; Khan, 2009). While the Shorten model does not estimate these biomarkers directly, various model components (ion distribution, tension, phosphate buildup) may be used to correlate with damage of the cellular structure. This damage can then be connected to increased concentrations of plasma biomarkers.

Links between muscle fiber contraction and clinical biomarkers have been identified. Extensive research in the exercise health community has evaluated muscle fiber damage following extreme muscle exertion. We have identified mathematical models and data sources describing this phenomenon that can be leveraged to establish a relationship between muscle fiber tension (estimated by the Shorten model) and subsequent muscle damage. The data on biomarkers of muscle fiber damage (myoglobin, CK, K+) from the controlled experiments will be useful in this work as well. Brumback et al. reported that “destruction of as little as 2 cc (2 g) of skeletal muscle tissue (about 10,000 muscle fibers) can result in a 10-fold increase over normal baseline values of the circulating (blood) levels of CK” (Brumback et al., 1995). This type of data could be used to correlate outputs of the excitation-contraction model to risk using a mechanistically-based dose response approach.

5. Summary and Conclusions

The goal of the HEMI project is to develop mechanistic models that can provide insight on the potential health risks from exposure to different types of HEMI devices and under different use cases. Although adverse health effects are rare under normal HEMI exposure conditions, some use cases may increase risk of health effects. Rhabdomyolysis is a known risk of HEMI exposure and in some cases can lead to kidney dysfunction and failure. Since renal injury is considered a serious injury and little has been done to characterize the risks of rhabdomyolysis with HEMI exposures, we have initially focused our efforts on modeling the risk of HEMI-induced rhabdomyolysis. To adequately model this risk, we are developing models of electrical dosimetry, motor neuron excitation, and muscle fiber excitation-contraction dynamics.

The electrical dosimetry model has been established through the solution of the electromagnetic Maxwell’s equations. While this is a simple concept in theory, solution to these equations can quickly become computationally burdensome when considering even simple 3D geometries. We have made significant progress simulating the electrical field for simple geometries and tissue properties using realistic HEMI device output as input to the dosimetry model. The model calculates the 3D electric field as a function of time throughout the geometry using the FDTD method. We can eventually pass this information to the SENN model, which will translate the electric field into recruitment volume by determining internal voltages and action potentials of motor neurons.

Calculation of the action potential (SENN model) is the intermediate step between the electrical dosimetry and muscle response models. The SENN model is a well-established mathematical representation of potential energy traversed across a neuron given an external electric field. Because the model is well developed, we have been able to run various simulations and analyses for this model, capturing the dependence of action potentials on external stimulation

characteristics. Of particular interest from our findings is the effect that the following three parameters have on the threshold current: the distance between electrodes (Figure 17), the distance between the electrodes and neuron (Figure 18), and the number of consecutive pulses (Figure 20). These dependencies will be important when evaluating the effect of various HEMI device characteristics and exposure profiles on recruitment volume.

We have chosen to use the Shorten model to simulate muscle fiber excitation-contraction dynamics. After acquiring and verifying this model, we have conducted a basic dose response of tension and myoplasmic calcium, dependent on characteristics of the applied electrical current. The output of the Shorten model establishes electrically-stimulated molecular and tension dynamics, which can be further used to correlate to muscular damage. The input of this model can be easily adapted to accept action potential information estimated by the SENN model. Connecting the SENN model to the electrical dosimetry model and Shorten model will establish an end-to-end system that predicts muscle response. Additional relationships can be established to relate model outputs to muscle damage and subsequent risk of rhabdomyolysis from exposure to a HEMI device.

6. Future

6.1. Model development

Future work is necessary to add complexity and accuracy to the dosimetry model in terms of geometric precision and resolution. Model stability must be confirmed at each step of the process. Once the tissue and source models sufficiently capture the specific properties of human tissue and HEMI devices, we will begin to test adding complexity to the computational geometry. To leverage existing data in swine, a swine-specific geometric model is necessary to complement the human model. Accurate, high-resolution 3D geometries for animals and humans must be identified. Efforts must continue to develop the most appropriate dose metric (e.g., current density, electric field, recruitment volume, potential) for integration with the motor neuron excitation model and dose response models. As the computational complexity of the electrical dosimetry model increases, it may also prove necessary to construct a library of model results gathered from a parametric study of the most important model inputs. This library could then be used in a more computationally efficient integrated rhabdomyolysis risk model which references the electrical dosimetry model output which was previously produced.

The SENN model in its present form calculates within 1% of the required threshold current by the device to generate an action potential. As a result, the solution may diverge if the initial estimate of the current is not near final value. Hence, a significant amount of trial and error may be necessary to obtain a solution. SENN model convergence may be improved by implementing new algorithms to allow a robust solution for the threshold current to improve model accuracy and reduce run times. The new model will allow for a more stringent convergence criteria far below 1% without sacrificing the run time. We would also like to link the SENN model to muscle response (Shorten) model to study the effect due to an exposed potential field from a HEMI device. The revised model could analyze the input potential to ensure that a sufficient action potential is achieved without reaching exposures that impose a health concern. Action potential in the target range will be passed on to the Shorten model for additional calculations and analysis. Communication between the SENN and Shorten models will be made by sending outputs to a data file with the required input parameters by the Shorten model.

The Shorten model, which we have chosen to simulate the excitation-contraction dynamics of skeletal muscle fibers, is a complex multi-component system. Each piece of this model can be expanded to improve the fidelity of different dynamics, but validation can become increasingly difficult as the model gains complexity. We will have started with simple models for each component, and expand on each one as necessary (see Section 4.3). The first priority for model expansion, however, is to alter and/or expand upon the model to allow for ATP depletion and intracellular calcium buildup. This is crucial in capturing the early pathophysiological processes leading to electrostimulation-induced rhabdomyolysis.

6.2. Model integration

After these models have been fully developed, they will be linked and integrated in a comprehensive tool (Figure 30). This tool should be capable of predicting the risk of rhabdomyolysis given any combination of device characteristics and exposure profiles. More details regarding our integration plan for these models are provided below.

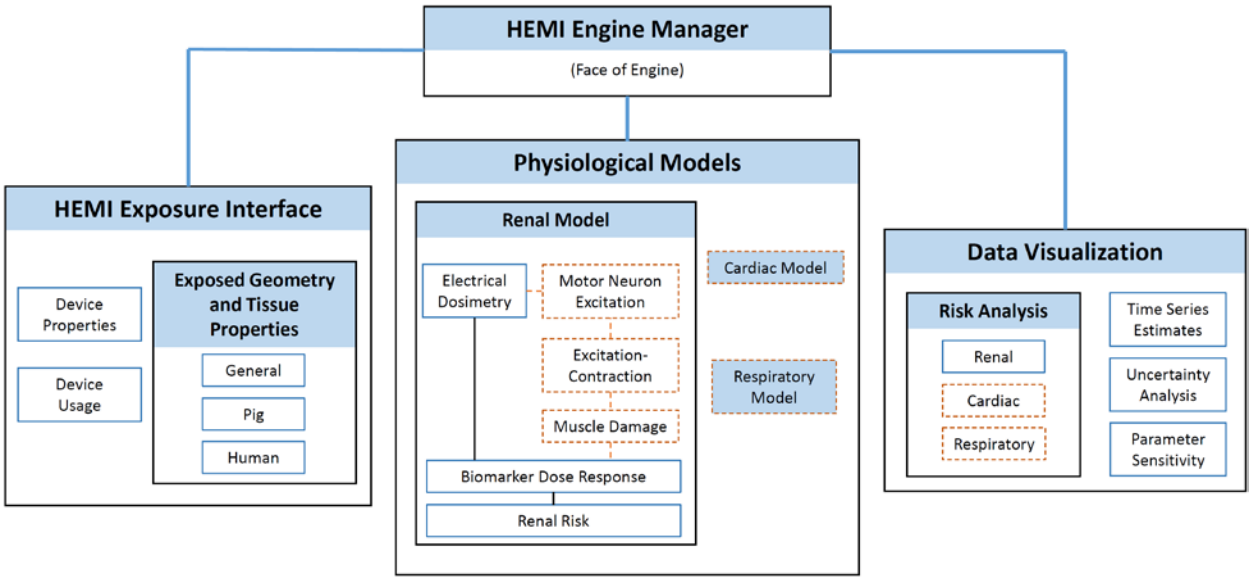

Figure 30. Short term and long-term (orange dashed) vision for the future modeling structure of the HEMI project.

A near-term goal for model integration must be to establish a dose-response for renal failure directly from the predictions of the electrical dosimetry model. This will be established by evaluating correlations between dose metrics (total recruitment volume, duration of exposure, susceptible tissue exposure, etc.) and biomarker levels, which can be validated using previously published data. This will provide the model with an initial end-to-end risk estimator that will serve as a higher-level risk model which can be used to guide the development of the more detailed mechanistic models (motor neuron excitation and muscle fiber excitation-contraction) and later aid in their validation.

The longer-term goal of the project is to integrate each of the mechanistic models, and use the high-fidelity outputs to correlate to biomarkers indicative of risk. Integrating these models will

require running them in a predefined sequence with the outputs of one model being fed into one or more models downstream. To facilitate this, a proof of concept tool will be created to facilitate setting up model inputs, running models in appropriate sequence, and viewing/exporting results. The standalone application will allow users to input basic parameters for a HEMI device with specific characteristics. Values for the physiological parameters of the individual will also be available for editing. These values will include parameters for the exposure (HEMI device characteristics, duration of exposure, location of electrodes, etc.) as well as the individual being exposed (height, weight, age, etc.). A concept for the input interface for "Physiological Parameters" is shown below.

Session Parameters | Physiological Parameters

Parameter	Value
Body Weight	85.0
Body Height	1.8
% Fatty Tissue	25
% Muscle Tissue	17
% Bone	21.0
Tissue Conductivity	50.0
Bone Density	80.0

Figure 31. Prototype GUI inputs for the dose response model.

After running the model, the user interface will show results in tabular form (similar to Figure 31) and in a series of graphs that the user can select from to get a quick overview of the simulation results (Figure 32). As shown in Figure 32, the available graphs would be listed on the left; selecting one would show the appropriate data set.

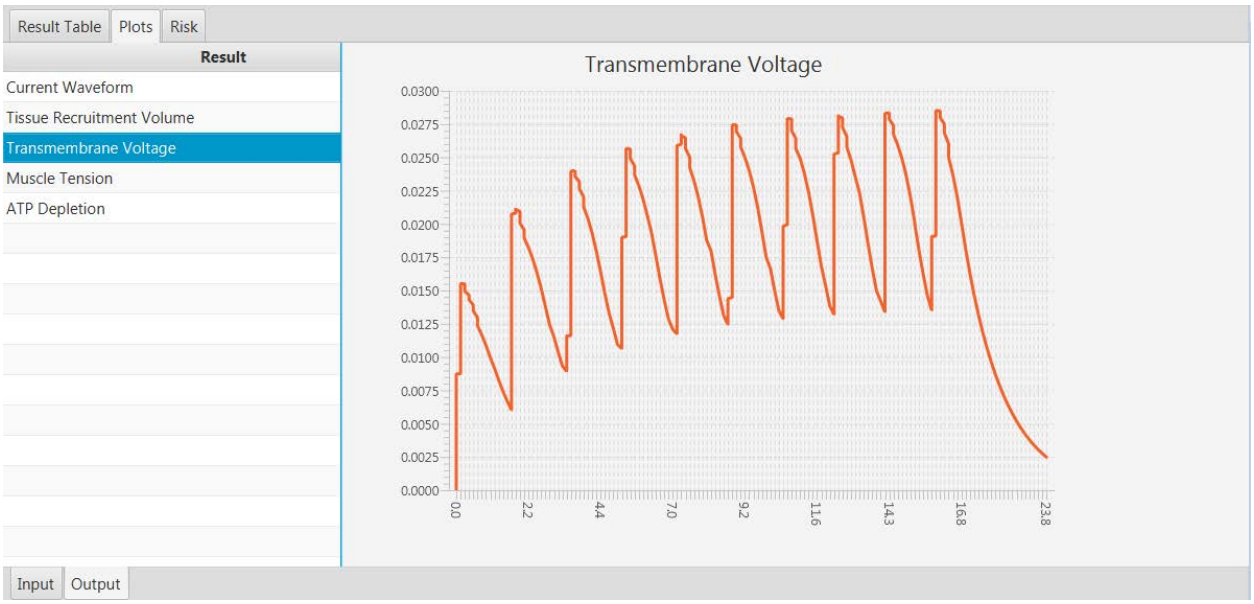

Figure 32. Prototype GUI outputs for the dose response model.

The GUI would also have features to save both the inputs and the outputs as an XLS file for more rigorous analysis by advanced users in the tool of their choice.

7. References

Andreuccetti, D., & Fossi, R. (2000). Dielectric properties of human tissues: definitions, parametric model, computing codes IROE Technical report N.

Arsac, L. M., Thiaudiere, E., Diolez, P., & Gerville-Reache, L. (2004). Parameter estimation in modeling phosphocreatine recovery in human skeletal muscle. *Eur J Appl Physiol, 91*(4), 419-424. doi: 10.1007/s00421-003-1001-5

Bergstrom, M., & Hultman, E. (1988). Energy cost and fatigue during intermittent electrical stimulation of human skeletal muscle. *J Appl Physiol (1985), 65*(4), 1500-1505. doi: 10.1152/jappl.1988.65.4.1500

Brumback, R. A., Feeback, D. L., & Leech, R. W. (1995). Rhabdomyolysis following electrical injury. *Semin Neurol, 15*(4), 329-334. doi: 10.1055/s-2008-1041040

Chance, B., Leigh, J. S., Jr., Clark, B. J., Maris, J., Kent, J., Nioka, S., & Smith, D. (1985). Control of oxidative metabolism and oxygen delivery in human skeletal muscle: a steady-state analysis of the work/energy cost transfer function. *Proc Natl Acad Sci U S A, 82*(24), 8384-8388.

Christ, A., Kainz, W., Hahn, E. G., Honegger, K., Zefferer, M., Neufeld, E., . . . Chen, J. (2009). The Virtual Family—development of surface-based anatomical models of two adults and two children for dosimetric simulations. *Physics in Medicine & Biology, 55*(2), N23.

Cooks, T., Davis, T. K., Hu, J., Metheny, R., Schwartz, M., & Gerona, R. (2016). "Smoking" guns: Questions. "Smoking" guns: Answers. *Pediatr Nephrol, 31*(1), 61-62, 63-66. doi: 10.1007/s00467-014-2978-1

Criddle, L. M. (2003). Rhabdomyolysis. Pathophysiology, recognition, and management. *Crit Care Nurse, 23*(6), 14-22, 24-16, 28 passim; quiz 31-12.

Dawes, D. M., Ho, J. D., Sweeney, J. D., Lundin, E. J., Kunz, S. N., & Miner, J. R. (2011). The effect of an electronic control device on muscle injury as determined by creatine kinase enzyme. *Forensic Sci Med Pathol, 7*(1), 3-8. doi: 10.1007/s12024-010-9187-4

Gabriel, C. (1996). Compilation of the Dielectric Properties of Body Tissues at RF and Microwave Frequencies: KING'S COLL LONDON (UNITED KINGDOM) DEPT OF PHYSICS.

Gissel, H. (2005). The role of Ca2+ in muscle cell damage. *Ann N Y Acad Sci, 1066*, 166-180. doi: 10.1196/annals.1363.013

Gleason, J. B., & Ahmad, I. (2015). TASER((R)) Electronic Control Device-Induced Rhabdomyolysis and Renal Failure: A Case Report. *J Clin Diagn Res, 9*(10), HD01-02. doi: 10.7860/JCDR/2015/15465.6608

Ho, J. D., & Dawes, D. M. (2011). TASER device-induced rhabdomyolysis is unlikely. *J Emerg Med, 40*(1), 68-69; author reply 69. doi: 10.1016/j.jemermed.2009.08.068

Huerta-Alardin, A. L., Varon, J., & Marik, P. E. (2005). Bench-to-bedside review: Rhabdomyolysis -- an overview for clinicians. *Crit Care, 9*(2), 158-169. doi: 10.1186/cc2978

Hultman, E., & Sjoholm, H. (1983). Energy metabolism and contraction force of human skeletal muscle in situ during electrical stimulation. *J Physiol, 345*, 525-532.

Karatzaferi, C., de Haan, A., Ferguson, R. A., van Mechelen, W., & Sargeant, A. J. (2001). Phosphocreatine and ATP content in human single muscle fibres before and after maximum dynamic exercise. *Pflugers Arch, 442*(3), 467-474.

Khan, F. (2009). Rhabdomyolysis: a review of the literature. *Neth J Med, 67*(9), 272-283.

Kim, J., Lee, J., Kim, S., Ryu, H. Y., Cha, K. S., & Sung, D. J. (2016). Exercise-induced rhabdomyolysis mechanisms and prevention: A literature review. *Journal of Sport and Health Science, 5*(3), 324-333.

Liebig, T., Rennings, A., Held, S., & Erni, D. (2013). openEMS–a free and open source equivalent-circuit (EC) FDTD simulation platform supporting cylindrical coordinates suitable for the analysis of traveling wave MRI applications. *International Journal of Numerical Modelling: Electronic Networks, Devices and Fields, 26*(6), 680-696.

Massey, J. W., & Yilmaz, A. E. (2016). AustinMan and AustinWoman: High-fidelity, anatomical voxel models developed from the VHP color images. *Conf Proc IEEE Eng Med Biol Soc, 2016*, 3346-3349. doi: 10.1109/EMBC.2016.7591444

McNeal, D. R. (1976). Analysis of a model for excitation of myelinated nerve. *IEEE Trans Biomed Eng, 23*(4), 329-337.

Moghtader, J., Brady, W. J., Jr., & Bonadio, W. (1997). Exertional rhabdomyolysis in an adolescent athlete. *Pediatr Emerg Care, 13*(6), 382-385.

Mordhorst, M., Heidlauf, T., & Röhrle, O. (2015). Predicting electromyographic signals under realistic conditions using a multiscale chemo–electro–mechanical finite element model. *Interface focus, 5*(2), 20140076.

Mustafa, S., Abbosh, A. M., & Nguyen, P. T. (2014). Modeling human head tissues using fourth-order Debye model in convolution-based three-dimensional finite-difference time-domain. *IEEE Transactions on Antennas and Propagation, 62*(3), 1354-1361.

NASA. (2018). Man-System Integration Standards. Vol. 1, Section 3: Anthropometrics. https://msis.jsc.nasa.gov/sections/section03.htm

Nevill, A. M., Jones, D. A., McIntyre, D., Bogdanis, G. C., & Nevill, M. E. (1997). A model for phosphocreatine resynthesis. *J Appl Physiol (1985), 82*(1), 329-335. doi: 10.1152/jappl.1997.82.1.329

Reilly, J. P., & Diamant, A. M. (2011). *Electrostimulation: theory, applications, and computational model*: Artech House.

Rohrle, O., Davidson, J. B., & Pullan, A. J. (2012). A physiologically based, multi-scale model of skeletal muscle structure and function. *Front Physiol, 3*, 358. doi: 10.3389/fphys.2012.00358

Röhrle, O., Neumann, V., & Heidlauf, T. (2016). The role of parvalbumin, sarcoplasmatic reticulum calcium pump rate, rates of cross-bridge dynamics, and ryanodine receptor calcium current on peripheral muscle fatigue: a simulation study. *Computational and mathematical methods in medicine, 2016*.

Russell, T. A. (2000). Acute renal failure related to rhabdomyolysis: pathophysiology, diagnosis, and collaborative management. *Nephrol Nurs J, 27*(6), 567-575; quiz 576-567.

Sanford, J. M., Jacobs, G. J., Roe, E. J., & Terndrup, T. E. (2011). Two patients subdued with a TASER(R) device: cases and review of complications. *J Emerg Med, 40*(1), 28-32. doi: 10.1016/j.jemermed.2007.10.059

Shorten, P. R., O'Callaghan, P., Davidson, J. B., & Soboleva, T. K. (2007). A mathematical model of fatigue in skeletal muscle force contraction. *J Muscle Res Cell Motil, 28*(6), 293-313. doi: 10.1007/s10974-007-9125-6

Singh, V., Ajeet, A., Kwatra, N., Cela, C. J., Ziriax, J., D'Andrea, J., & Lazzi, G. (2010). Computation of induced current densities in the human body at low frequencies due to contact electrodes using the ADI-FDTD method. *IEEE Transactions on Electromagnetic Compatibility, 52*(3), 537-544.

Soderlund, K., & Hultman, E. (1991). ATP and phosphocreatine changes in single human muscle fibers after intense electrical stimulation. *Am J Physiol, 261*(6 Pt 1), E737-741. doi: 10.1152/ajpendo.1991.261.6.E737

Torres, P. A., Helmstetter, J. A., Kaye, A. M., & Kaye, A. D. (2015). Rhabdomyolysis: pathogenesis, diagnosis, and treatment. *Ochsner J, 15*(1), 58-69.

Visweswaran, P., & Guntupalli, J. (1999). Rhabdomyolysis. *Crit Care Clin, 15*(2), 415-428, ix-x.

Wrogemann, K., & Pena, S. D. (1976). Mitochondrial calcium overload: A general mechanism for cell-necrosis in muscle diseases. *Lancet, 1*(7961), 672-674.

Yee, K. (1966). Numerical solution of initial boundary value problems involving Maxwell's equations in isotropic media. *IEEE Transactions on Antennas and Propagation, 14*(3), 302-307.

Zhang, M.-h. (2012). Rhabdomyolosis and its pathogenesis. *World journal of emergency medicine, 3*(1), 11.